COMPARISON OF VORTEX AND CAVITATION CHARACTERISTICS OF HYDRAULIC MACHINERY IN TRANSLATIONAL AND ROTATIONAL DOMAINS

Jianbo ZANG[1,2], Hu ZHANG[1 *], Jun WANG[1], Desheng ZHANG[2], Fang AN[1], Kun CHENG[1]

[*1]School of Mechanical engineering, Wuxi Institute of Technology, Wuxi, China
[2]Research Center of Fluid Machinery Engineering and Technology,
Jiangsu University, Zhenjiang, China
[*] Corresponding author; E-mail: zhanghutianxia@126.com

To investigate the differences and similarities in vortex and cavity characteristics between translational and rotational domain hydraulic machines, the NACA0009 hydrofoil and a self-designed impeller blade were selected as representative cases in the translational and rotational domains. STAR-CCM+ software was utilized to simulate the multiphase flow, and the experimental results of NACA0009 hydrofoil from EPFL were employed to validate the accuracy of the simulation. The following conclusions were drawn from the analysis of the simulation results: Firstly, both types of hydraulic machinery generate similar vortex types, including the tip leakage vortex (TLV), tip separation vortex (TSV), and secondary tip leakage vortex (S-TLV). However, each type also exhibits unique vortices, such as the perpendicular vortex (PV) in the translational domain and the trailing edge vortex (TEV) in the rotational domain. Secondly, the TLV is initially weak but continuously absorbs other vortices, thereby strengthening itself as it develops. Additionally, the blades in the rotational domain must achieve a higher speed to produce the same level of cavitation as those in the translational domain. Finally, the attached cavitation (AC) on the blade surface is repelled by the spin of the TLV, which cannot promote the generation of tip leakage vortex cavitation (TLVC). The primary source of TLVC is the tip separation vortex cavitation (TSVC). The strengths of cavitation and vortices differ between the rotational and translational domains, leading to varying effects on the equipment.

Key words: *hydraulic machinery, numerical simulation, vortex, cavitation*

1. Introduction

Vortex and cavitation in hydraulic machinery are two critical hydrodynamic phenomena that significantly impact engineering applications. Vortex is typically defined as a region of rotating flow created by the movement of fluid. This phenomenon can lead to several undesirable effects, including reduced equipment performance, increased vibration, and potential damage to mechanical components. Additionally, the formation and development of vortices can result in flow separation, which may subsequently cause vortex cavitation. The emergence, growth, and eventual collapse of cavities can lead to decreased equipment performance, elevated noise levels, and even wear on blade surfaces. These phenomena are associated with the instability of fluid motion and dynamic pressure fluctuations, particularly under conditions of high-speed flow or significant pressure differentials. Therefore,

effective management of vortices and cavitation is essential to ensure the safe operation and long-term reliability of hydraulic machinery.

Xie *et al.* [1] demonstrated that the generation and shedding of vorticity during tidal power generation would result in sudden changes in the hydrodynamics of a hydrofoil, which would dissipate the tidal energy captured by the hydrofoil and reduce the efficiency of energy capture. Xu *et al.* [2] investigated the relationship between the attached vortex on a hydrofoil and the lift force of the hydrofoil. Zhang *et al.* [3] conducted experiments to investigate the cavitating fluid-structure interaction of composite hydrofoils with different ply angles. Liu *et al.* [4] employed various turbulence models to examine the cloud cavitation state around Clark-Y hydrofoils and compared the results with experimental data. Liu *et al.* [5] examined the interaction between cavities and vortices in NACA0009 flexible hydrofoils by integrating simulation and experimentation. Dular *et al.* [6] employed computer-aided image processing to quantify cavitation erosion in hydrofoils and established a relation between the characteristics of cavitation structures and cavitation damage. Kumagai *et al.* [7, 8] and Murai *et al.* [9] investigated the phenomena of wave breaking and bubble generation on the free surface of two-dimensional cylinders during movement and developed a device used as a bubble generator for drag-reducing ships, which demonstrated effective drag reduction. Zhang *et al.* [10] and Zang *et al.* [11] investigated the cavitation shedding and evolution mechanism on the surface of twisted hydrofoils, and emphasized the role of re-entrant jet on cavity shedding. Zhang *et al.* [12] proposed a practical method to suppress noise near the capillary outlet by studying the two-phase flow characteristics of refrigerant in the transition pipe. Hutli *et al.*[13] researched the dependency of the jet power and the cavitation intensity on the working conditions of the cavitating and non-cavitating jet flow. Qin *et al.* [14] conducted a numerical analysis of the separated vortex simulation to study the vortex instability of the wake of the preswirl pumpjet propulsor. Zhang *et al.* [15] employed vortex generators in front of the impeller to investigate the changing trend of the inlet vortex and its influence on the axial flow pump. Zhang *et al.* [16] applied the Omega method to investigate the behaviour of reversible pump turbines. This approach enabled the identification and comparison of vortices under various operational modes. Zhang *et al.* [17] has identified the shape and distribution of vortices in axial flow pumps based on Q criteria and the Liutex method, and analysed the interaction between impeller and vortices. The findings of Shi *et al.* [18] indicated that an increase in cavitation would have a significant negative impact on the performance parameters of the pump. Song *et al.* [19] employed an experimental approach in conjunction with numerical simulation to investigate the pressure characteristics of floor adhesion vortex FAV and its influence on the pump. Long *et al.* [20] conducted research into the characteristics of cavitation wake vortex structures by combining experiment and numerical simulation. This research discussed the influence of the cavitation region of tip leakage vortex TLV and impeller suction surface on the structure of the cavitation wake vortex at different stages of cavitation. Lu *et al.* [21, 22] undertook research into the formation and development of cavitation in centrifugal pumps, and analysed the flow characteristics and pressure pulsation changes in pumps under cavitation conditions. Zhao *et al.* [23] attempted to prevent the generation of cavitation in a centrifugal pump by adding barrier blocks to the blade.

These scholars conducted research on the vortex and cavitation characteristics of hydrofoils, pumps, and other hydraulic machinery, and put forward their own views about them. Their work encompasses the impact of vortex and cavitation generation and shedding on equipment performance, the interplay between cavitation and vortex, and the influence of equipment structure on the genesis of

both phenomena. Nevertheless, their studies on vortex and cavitation are limited to the analysis of specific fluid machinery, namely translational domain machinery, such as hydrofoils, and rotational machinery, such as pumps. There is a paucity of research investigating the distinctions in the characteristics of vortex and cavitation between these two hydraulic machinery. In order to conduct a comprehensive investigation into this issue, this paper will use NACA0009 as a case study for the translational domain and a self-designed impeller blade as a case study for the rotational domain. The findings of this research project regarding the similarities and differences in the characteristics of vortex and cavitation across various types of fluid machinery will serve as a point of reference for subsequent research in this field.

2. Fundamental governing equation

2.1. Continuity equation and momentum equation

This paper employs the Reynolds Average Navier-Stokes method(RANS), to conduct both steady-state and transient-state numerical simulations. This method ignores the effects of turbulence pulsation at all scales and only solves the average motion, thus greatly shortening the calculation time. The governing equation comprises a continuity equation and a momentum equation, expressed as follows:

$$\frac{\partial \rho}{\partial t}+\frac{\partial(\rho u_j)}{\partial x_j}=0 \tag{1}$$

$$\frac{\partial u_i}{\partial t}+\frac{\partial(u_i u_j)}{\partial x_j}=-\frac{1}{\rho}\frac{\partial p}{\partial x_i}+\frac{1}{\rho}\frac{\partial}{\partial x_j}(\mu\frac{\partial u_i}{\partial x_j})+f_i \tag{2}$$

Where ρ is the density, u is the velocity, p is the pressure, μ is the dynamic viscosity, i, j can take values of 1, 2, 3, representing x, y, z, respectively, f_i represents the volume force term, such as gravity.

2.2. Turbulence model equation

Given that the turbulent viscosity μ_t in the momentum equation is unknown, it is necessary to introduce a turbulence model in order to solve for its value. The turbulence model employed in this paper is the SST k-ω turbulence model[24], which combines the respective advantages of k-ω turbulence model and the k-ε turbulence model. The mixed function F_1 is introduced as the control, and the k-ω turbulence model is employed to calculate the viscous bottom layer directly on the near wall, while the k-ε turbulence model is used to enhance stability on the far wall. On this basis, the mixing function F_2 is introduced to correct the turbulent viscosity μ_t, so as not to overpredict the viscosity. The governing equation is as follows:

$$\frac{\partial(\rho k)}{\partial t}+\frac{\partial}{\partial x_j}(\rho u_j k)=\frac{\partial}{\partial x_j}\left[\left(\mu+\frac{\mu_t}{\sigma_k}\right)\frac{\partial k}{\partial x_j}\right]+P_k-C_\mu\rho k\omega \tag{3}$$

$$\frac{\partial(\rho\omega)}{\partial t}+\frac{\partial}{\partial x_j}(\rho u_j\omega)=\frac{\partial}{\partial x_j}\left[\left(\mu+\frac{\mu_t}{\sigma_\omega}\right)\frac{\partial\omega}{\partial x_j}\right]+\alpha\frac{\omega}{k}P_k-\beta\rho\omega^2 +2\rho(1-F_1)\frac{1}{\sigma_\omega\omega}\frac{\partial k}{\partial x_j}\frac{\partial\omega}{\partial x_j} \tag{4}$$

$$P_k=\mu_t\left(\frac{\partial u_i}{\partial x_j}+\frac{\partial u_j}{\partial x_i}\right)\frac{\partial u_i}{\partial x_j} \tag{5}$$

Among these, C_μ, α, β, σ_ω, σ_k are empirical constants, and their sizes can be dynamically weighted by F_1.[26]

2.3. Cavitation model equation

In this study, the Schnerr-Sauer cavitation model is employed[25], wherein the phase transition rate is expressed as follows:

$$\dot{m}^+=F_{\text{vap}}\frac{\rho_l\rho_\text{v}}{\rho}\alpha_\text{v}(1-\alpha_\text{v})\frac{3}{R_\text{B}}\sqrt{\frac{2}{3}(\frac{p_\text{v}-p}{\rho_l})} \quad p \text{ ,, } p_\text{v} \tag{6}$$

$$\dot{m}^-=F_{\text{cond}}\frac{\rho_l\rho_\text{v}}{\rho}\alpha_\text{v}(1-\alpha_\text{v})\frac{3}{R_\text{B}}\sqrt{\frac{2}{3}(\frac{p_\text{v}-p}{\rho_l})} \quad p>p_\text{v} \tag{7}$$

$$R_\text{B}=\left(\frac{\alpha_\text{v}}{1-\alpha_\text{v}}\frac{3}{4/\pi}\frac{1}{n_0}\right)^{\frac{1}{3}} \tag{8}$$

In the case where the saturated vapor pressure p_v=3170Pa, seed density n_0=1×10^{12}, R_B is the bubble radius. F_{vap} and F_{cond} are respectively the evaporation and condensation coefficients. The default values in STAR-CCM+[26] are both 1.

3. Geometric model and boundary conditions

3.1. Translational domain

In the section of the paper concerning the translational domain, the NACA0009 hydrofoil case study presented by Dreyer *et al.* [27,28] is employed as a reference. This case will produce very typical vortex structure and cavitation phenomenon. At the same time, detailed experimental data, including cavitation images and velocity field data, are disclosed in the paper to verify the accuracy of the simulation results. In this paper, a case with the most significant cavitation and vortex is selected, the geometric dimensions and boundary conditions are illustrated in Fig. 1. The section of the airfoil is NACA0009, the chord length is 100mm, the wingspan is 140mm, the angle of attack is 10°, and there is a gap of 10mm between one side and the wall. In the experimental verification case, the pressure edge is rounded to aradius of 1mm. The length of the basin is 750mm, the inlet and outlet are 150mm ×150mm rectangular, and the distance between the hydrofoil and the inlet is 200mm. The inlet velocity V_{inlet}=10m/s, and the outlet pressure p_{outlet}=1bar. With the exception of the side wall on the gap side, which is non-slip wall, the remaining three side walls are sliding walls.

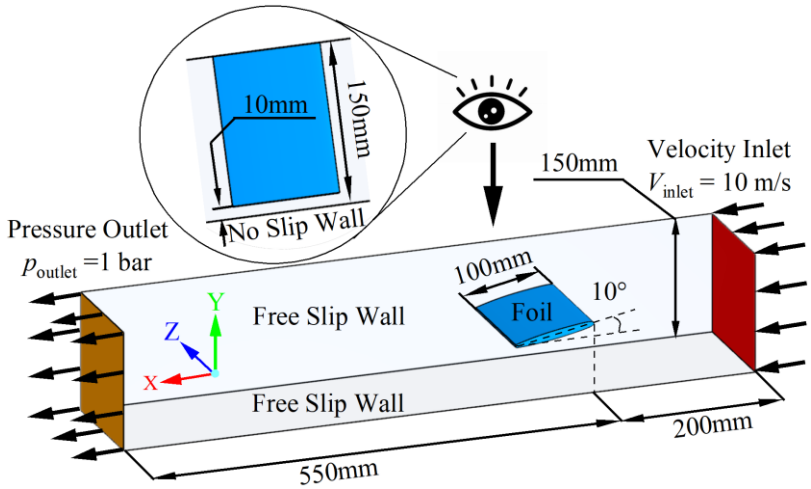

Figure 1. Hydrofoil geometric parameters and boundary conditions

3.2. Rotational domain

A comparative study of vortex and cavitation in the translational and rotational domains necessitates the design of an impeller with analogous parameters for the NACA0009 hydrofoil, as illustrated in Fig. 2. The impeller is constituted by a single blade, the outermost chord length is 100 mm, the angle of attack is 10°, and the gap with the side wall is 10 mm, in order to ensure that the parameters in the two domains are consistent as far as possible. The rotational domain case presented in this paper is conducted within the impeller hydraulic performance test apparatus, as show in Fig. 3(a). The device was designed by our team based on the axial flow pump, and its structure was greatly simplified. The internal blade is made by 3-D printing for easy replacement, which allows for the analysis of the influence of different design parameters on the hydraulic performance of the impeller. The boundary conditions of the impeller hydraulic performance test apparatus are defined as illustrated in Fig. 3(b). The flow field is comprised of three domains: the rotational domain, the water domain, and the air domain. Internal interfaces are added between each domain. With the exception of the symmetric plane used for the opening, all other planes are set as non-slip wall surfaces. The the working pressure p_0 is set at 1bar, with the rotational domain and the water domain are set as rotation. At the rotational speed n of 1200r·min^{-1}, 1800r·min^{-1}, 2100r·min^{-1} and 2400r·min^{-1}, the blade tip velocity V_{tip} can reach 11.31m·s^{-1}, 16.96m·s^{-1}, 19.79m·s^{-1} and 22.62m·s^{-1}, respectively. This is then compared with the working condition of 10m·s^{-1} in the translational domain.

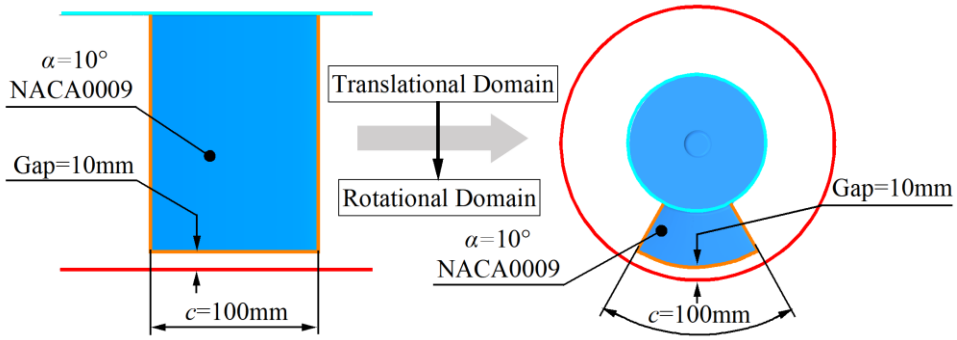

Figure 2. Parameter diagram of translational domain and rotational domain

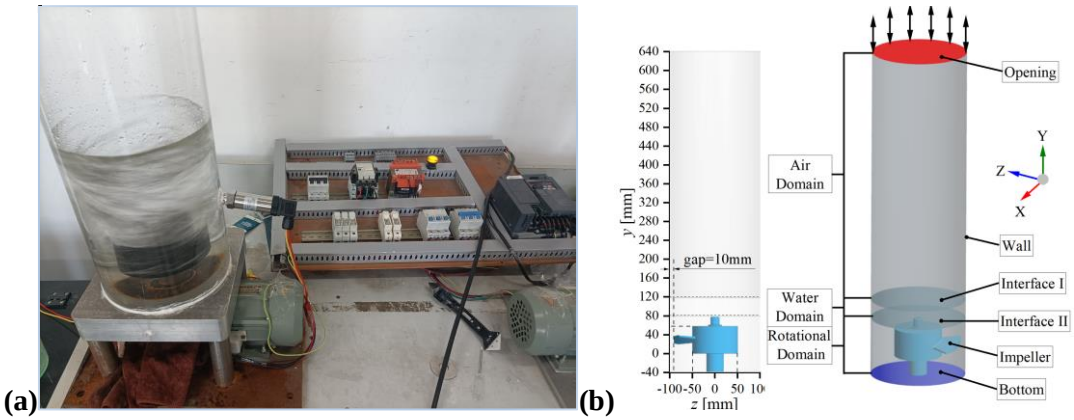

Figure 3. (a)the impeller hydraulic performance test apparatus
(b)Geometrical parameters and boundary conditions of the rotational domain

4. Simulation result verification

4.1. Translational domain verification

The solver employed in this study is STAR-CCM+ 2306[26], which features a robust mesh adaptive partitioning function that can effectively reduce the time spent on grid partitioning. This study employs the experimental data from Dreyer [27, 28] as a benchmark to validate the accuracy of the software. Furthermore, three distinct schemes were developed for comparative analysis. Schemes 1 and 2 employed software ANSYS ICEM to generate hexahedral grids, which were separately imported into STAR-CCM+ and ANSYS CFX for solution. Scheme 3 utilised polyhedral grids, which were divided by STAR-CCM+. The distribution of correlation grids in horizontal and vertical directions is shown in Fig. 4, he upper left corner is hexahedral structured grid generated using ANSYS ICEM, and the lower right corner is a polyhedral grid generated by STAR-CCM+. Both are encrypted at the gap, but the STAR-CCM+ encryption is more flexible, with the case used in this paper encrypting the gap twice according to the importance of the actual situation. In comparison with ANSYS ICEM, the STAR-CCM+ mesh partitioning method allows users to adjust the mesh density distribution flexibly, effectively reducing the time and number of mesh partitions, and the burden on users and computers.

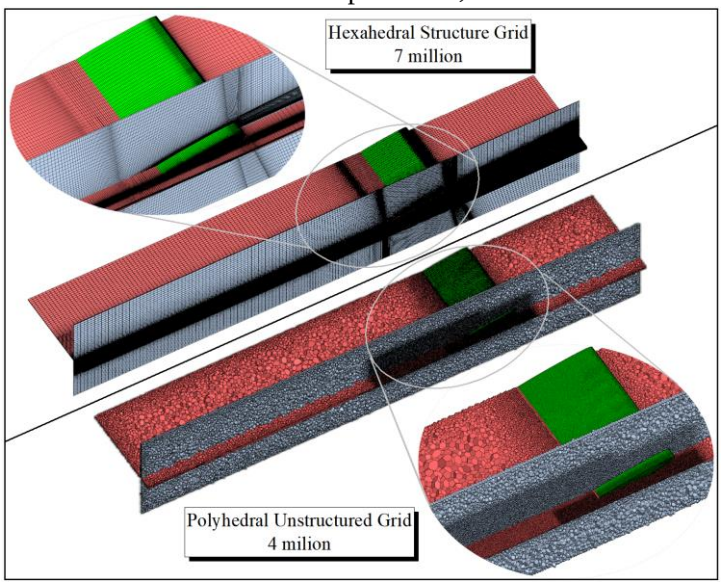

Figure 4. Hydrofoil grid division diagram

Figure 5a depicts the velocity cloud image of the cross-sectional flow direction (x-direction) at x/c=1 downstream of the hydrofoil. It can be observed that although the total number of polyhedral grids divided by STAR-CCM+ is not as optimal as the structured grids of ANSYS ICEM, its accuracy can still meet the necessary requirements after careful encryption by users. The simulation results obtained without cavitation are used as initial values to solve the cavitation conditions. The results are presented in Fig. 5b, which demonstrates that the simulated TLV cavitation is consistent with Dreyer's experimental results[27,28]. Given the good performance of STAR-CCM+ in hydrofoil simulation, the rotation domain is also simulated using this software.

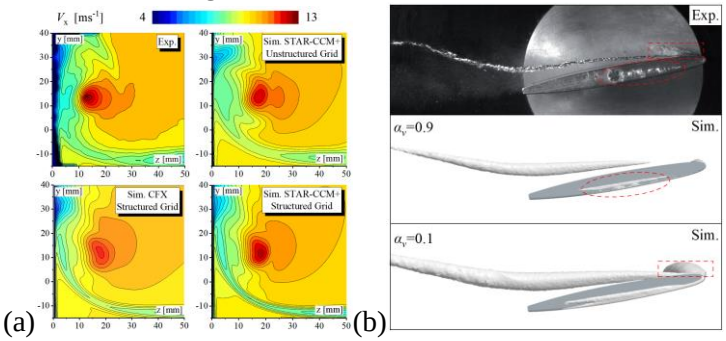

(a) (b)

Figure 5. (a) no cavitation velocity cross section (b) cavitation contour[27,28]

4.2. Rotational domain verification

Four grid division methods were employed to generate distinct grids for the rotating field experimental equipment. Among these, grids 2, 3, and 4 were subjected to local encryption, while grids 3 and 4 were globally encrypted to varying degrees on the basis of grid 2. The grid distribution is illustrated in Fig. 6a.

Figure 6b illustrates the grid-independent distribution of the four sets of grids at varying speeds, including the lift curve generated by the impeller and the flow field at 0.25s. Following a comparative analysis, it can be observed that the lift curves of grids 3 and 4 exhibit the greatest consistency, with the liquid surface heights being almost identical. Given the computational time constraints, the simulation data of grid 3 is ultimately selected for further processing.

Figure 6c illustrates the gas-liquid interface state between the experimental device and the simulator at three different rotational speeds. The similarity between the two is notable, including the liquid column height and shape, which provides a degree of assurance regarding the accuracy of the simulation.

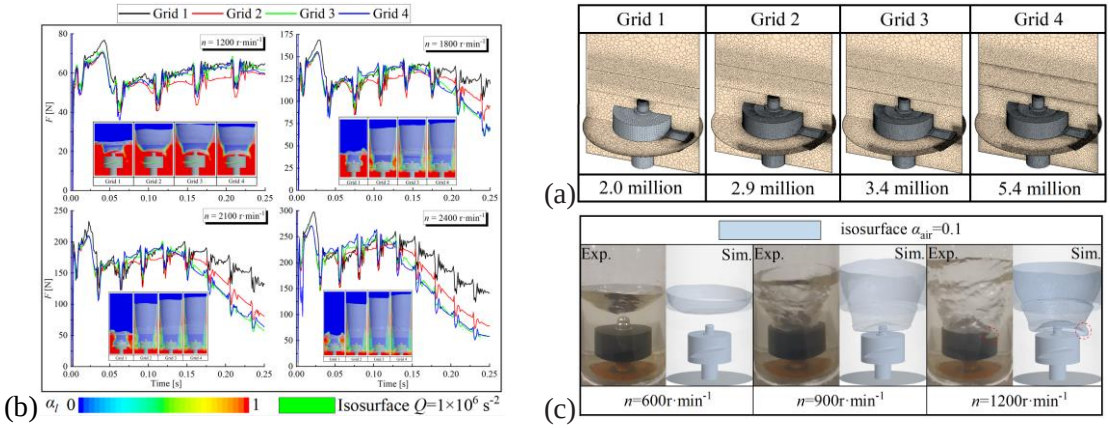

(b) (a) (c)

Figure 6. Simulation result verification; (a) grid distribution
(b) grid independence verification (c) comparison of phenomena

5. Analysis of numerical simulation results

5.1. Vortex contrast

Figure 7 illustrates the vortex structure and the velocity distribution of the vortex surface at different velocities in the translational and rotational domains, respectively. As shown in Fig. 7a, when the inlet velocity of the translational domain (V_{inlet}=5m·s^{-1}), the Tip Leakage Vortex (TLV) [29] exhibits an obvious vortex structure, although its intensity is relatively weak. Concurrently, a considerable number of Tip Separation Vortexes (TSVs) [30] accumulate at the tip of the blade. These normally develop into Secondary Tip Leakage Vortex (S-TLV) [31] in the middle of the blade. However, due to the entrainment effect of TLV, S-TLV is carried away from the surface of the blade and cannot form a stable structure. However, the strength of TLV at this time is still relatively weak, so it is unable to absorb the S-TLV, so S-TLV only rotates around the movement path of TLV. When the import speed Vinlet is further increased to 7m·s^{-1}, TLV, S-TLV and TSV are all enhanced, and TLV has been able to absorb part of S-TLV to strengthen itself, thus extending its development distance. Secondly, the enhancement of TSV results in its distribution spreading to the rear of the tip. Under the influence of leakage flow, the redundant TSV turns into the second S-TLV (S-TLV-II) at the tail of the hydrofoil. This vortex's direction undergoes a change from a horizontal direction to a vertical direction as a consequence of the enrolling action of TLV. This vortex was designated as the Perpendicular Vortex (PV)[32-34]. At inlet velocities of 10m·s^{-1} and 12m·s^{-1}, TLV absorbs TSV at the blade tip to strengthen itself, resulting in a significant increase in strength and potential for further development. In contrast, S-TLV lacks the space to develop and its structure is invisible. As the increase in flow velocity will directly lead to an increase in TSV generation, the absorption of TLV also reaches its the upper limit, TSV covers the tip of the blade, and the TSV at the back of the tip is all absorbed by PV, which is greatly enhanced. Even if PV is entrained by TLV, it cannot be completely absorbed, and a certain PV structure can still be maintained.

The development of vortex in the rotation domain differs from that in the translational domain. As illustrated in Fig. 7b, when the rotational speed is n=1200r·min^{-1}, the tip velocity V_{tip} reaches 11.31m·s^{-1}, which is similar to the flow situation in the case where the inlet velocity V_{inlet}=5m·s^{-1}. However, the TLV intensity is considerably weaker than that observed in the translational domain. In contrast to the case of V_{inlet}=5m·s^{-1}, a weaker TLV allows for the development of S-TLV in a position analogous to the translational domain, with a markedly enhanced intensity. In contrast to the translational domain, the vortex at the trailing edge is driven toward the tip of the blade by the centrifugal force present in the rotational domain. Upon vortex reaches the tip of the blade, it is no longer protected by the trailing edge and begins to move, driven by the gap leakage flow, ultimately becoming the Trailing Edge Vortex (TEV). The TEV can be divided into two parts. The upper TEV is subject to stronger leakage flow, which results in a greater strength of TEV. Furthermore, the strength of TEV is positively correlated with the leakage intensity. In contrast, the strength of the lower TEV is not significantly influenced by the leakage flow, and its strength is not contingent on the impeller speed. It is generated exclusively by centrifugal force and cannot be augmented by leakage flow. By contrast, the absence of centrifugal force in the translational domain precludes the formation of TEV structures. Upon increasing the rotational speed to n=1800r·min^{-1}, the tip velocity reaches 16.96m·s^{-1}, This is accompanied by an increase in the intensity of the TLV, S-TLV, TEV and TSV, which can be attributed to the influence of enhanced leakage flow. Moreover, the S-TLV, TEV and the original TLV

are intermixed in the posterior region of the blade, with the vorticity continuously transmitted from the other vortices to the original TLV. This results in a more powerful TLV. As the clearance leakage flow increases, the number of TSVs generated and occupying positions also rises. Concurrently, the position of S-TLV generation gradually shifts backwards, accompanied by a corresponding backward movement of the position of TLV absorption. Upon further increasing the rotational speed to n=2100r·min^{-1}, the S-TLV and TEV are absorbed by TLV at the same position. At n=2400r·min^{-1}, TLV is greatly enhanced, and TSV can be directly absorbed from the tip of the blade, with the generation of S-TLV no longer possible.

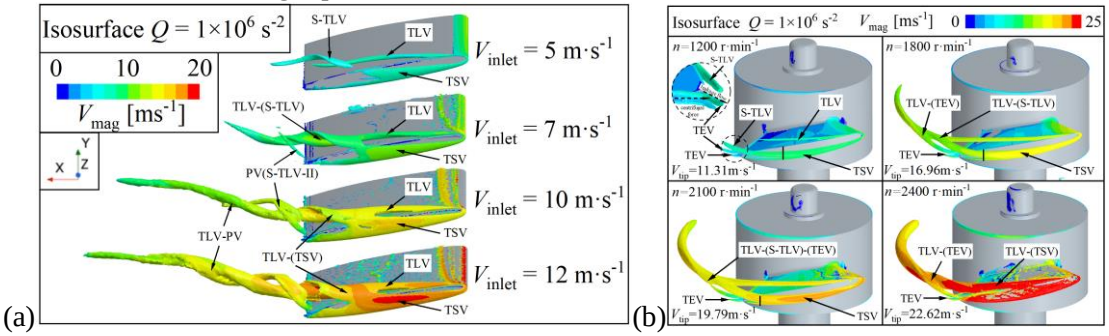

Figure 7. Vortex surface velocity; (a) translational domain (b) rotational domain

5.2. Cavitation contrast

Given that the rotational domain experimental equipment designed by our team in this paper is already a gas-liquid two-phase flow, the use of the cavitation model in its direct form will result in the three phases of vapour, air and water interacting. This will considerably increase the complexity of the simulation and reduce the stability of the calculations. Under normal circumstances, just like the translational domain, we will use the stable flow field data without cavitation as the initial value, and then conduct the numerical simulation of the flow field with cavitation, which can effectively improve the accuracy of the numerical simulation and ensure convergence. However, for our rotating domain device, it also involves the gas phase, even if cavitation model is not used, the simulation of the interaction between water and air will lead to strong transient characteristics of the flow field, which means that we cannot provide a stable flow field data as an initial value for simulation with cavitation. Therefore, a new method is proposed in this paper. Firstly, a gas-liquid two-phase transient simulation of the device is conducted, during which the lift curve and associated phenomena are observed and recorded. Subsequently, the air domain within the flow field is removed, and a single-phase steady-state simulation is carried out in place of a multi-phase steady-state simulation. This approach allows for the enhancement of the stability of the simulation. Finally, the flow fields of steady-state and transient simulations were compared. An iteration that is as close as possible to the transient flow field was selected as the initial value for the cavitation calculation. Figure 8 illustrates the lift curve, vortex structure, and relevant data of the gas-liquid interface for the two simulation methods.

As illustrated in the accompanying Fig. 8, when the liquid level reaches the surface of the impeller, the lift force generated by the impeller is significantly diminished, and the intensity of the vortex is also reduced due to the infiltration of air. When t<0.1s, the liquid level changes are not significant at the three high rotational speeds, the lift is stable, and the vortex structure is at its strongest state. In contrast, in the case of n=1200r·min^{-1}, the vortex develops to a relatively completely until 0.2s. A comprehensive comparison was conducted between the lift curve, vortex structure, and

gas-liquid interface of the two simulation methods under different speed conditions. The appropriate steady state results without cavitation were selected as the initial values to simulate the flow field with cavitation.

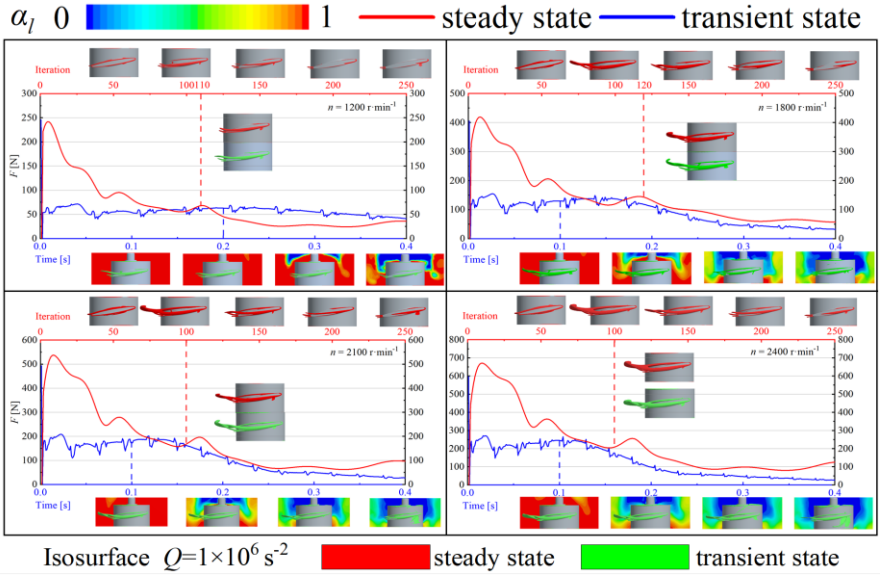

Figure 8. Steady state initial value selection for cavitation simulation

Figure 9 illustrates the cavitation isosurface and theoretical circumaxial velocity of the blade surface of the vortex generator under four rotational speeds. At a rotational speed is 1200r·min^{-1}, while the velocity at the tip of the blade can reach 11.31m·s^{-1}, this velocity threshold cannot be reached at other locations, resulting in a pressure drop that is insufficient to meet the cavitation requirements. Consequently, only a small, almost invisible void mass was formed at the leading edge of the tip. As the rotational speed increased to 1800r·min^{-1}, the tip velocity reached 16.96m·s^{-1}, and the Tip Separation Vortex Cavity (TSVC) began to take shape. The region of theoretical circumferential velocity $V_{c\infty}$>14m·s^{-1} on the suction surface generated Attached Cavity (AC)[35]. As the rotational speed was increased to 2100r·min^{-1}, the circumferential velocity at the tip of the blade reached 19.79m·s^{-1}, and the distribution range of TSVC was found to have increased. All parts of $V_{c\infty}$>12m·s^{-1} on the suction surface generate AC, almost covering the front of the blade. Upon reaching the rotational speed reaches 2400r·min^{-1}, the tip velocity reaches 22.64m·s^{-1}, resulting in the generation of a considerable amount of TSVC at the tip of the blade. This subsequently forms a Tip Leakage Vortex Cavity (TLVC) upon being sucked up by TLV. At this speed, the blade suction surface experiences a significantly higher velocity than 12m·s^{-1}, resulting in a substantial pressure drop. This leads to the generation of a considerable quantity of AC, which occupies approximately half of the suction surface.

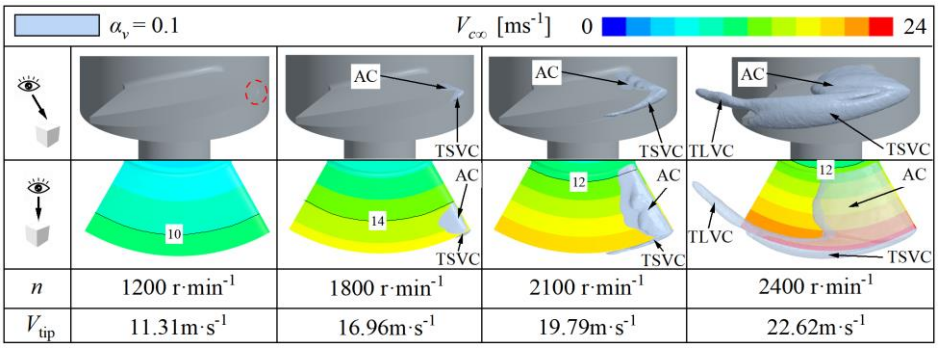

Figure 9. Blade cavitation distribution at different rotational speeds in rotational domain

Figure 10 illustrates the comparative analysis of cavitation phenomena in the translational and rotational domains at varying speeds. As illustrated in Fig. 10a, the increase in rotational speed results in a significant rise in the AC on the suction surface of the blade. However, the TLV exerts a repulsive influence on the AC on the suction surface due to its spin velocity. Concurrently, the rotation domain will impart a centrifugal force upon the fluid and the cavity. The combined action of these two forces results in the accumulation of AC on the suction surface in the radial middle of the blade, which cannot be absorbed by TLV. Therefore, the existence of AC does not greatly promote the formation of TLVC. It can be observed that there are two principal factors involved in the generation of TLVC. The first of these is TLV, while the second is TSVC. In order for the entrainment effect of TLV to be effective on TSVC, it is necessary that the TLV is in close proximity to the tip of the blade, that the TLV strength is sufficiently large, and that the TSVC can be extended to the position affected by TLV entrainment.

Since the generation of TLV is primarily dependent on the tip leakage flow[29], and as a result, its intensity increases with the position of the string length. As illustrated in Fig. 10b, when the incoming flow velocity is V_{inlet}=9m·s^{-1}, the intensity of the gap leakage flow is low, and the growth rate of TLV is slow. An increase in the velocity of the inlet results in a strengthening of the initial strength of TLV, an acceleration of the growth rate, and a faster reaching of the intensity threshold for absorbing TSVC. Consequently, the position of TLVC at birth is gradually advanced. Nevertheless, the strength of TLVC generated by this method remains relatively low. As previously stated, the nascent TLV will gradually strengthen itself by absorbing other vortex systems on numerous occasions, and thus will TLVC. The initial position of TSVC is at the lower side of the tip of the blade. However, under the influence of incoming flow and leakage jet, TSVC will move backward along the tip of the blade, gradually strengthening until it reaches the upper side of the tip. At this point, the well-developed TSVC will suddenly be absorbed by TLV, enhancing the intensity of TLVC at this position.

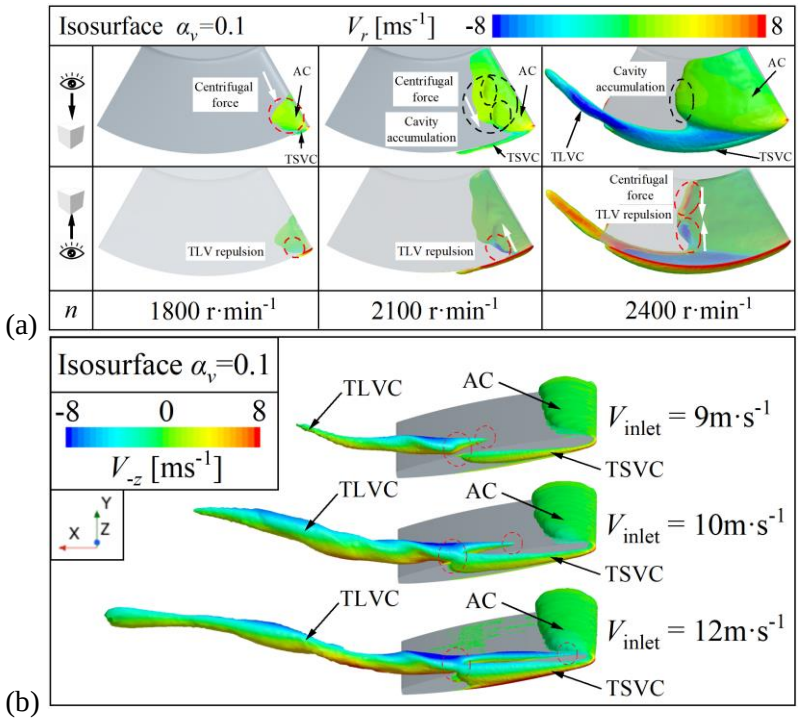

Figure 10. Cavity surface radial velocity; (a) rotational domain (b) translational domain

In conclusion, it can be stated that as long as the flow rate reaches the threshold, hydraulic machinery in both the rotational domain and the translational domain will generate a certain degree of vortex and cavitation in its interior. However, since the circumferential velocity of the rotational domain is not uniformly distributed along the radial direction, even if the velocity at the tip of the rotating domain reaches the same level as that of the translational domain, its vortex strength and cavitation degree are significantly less than that of the translational domain. It is more probable that hydrofoil structures in the translational domain will form high-strength cavitation and vortex than those in the rotational domain. However, the vortex and cavitation in the translational region mach will move along the flow path under the action of the inlet flow. This will result in the cavitation weakening its erosion effect on the hydrofoil structure after being pushed away from hydrofoil. Furthermore, the direction of the vortex in the translational domain is aligned with that of the flow channel, which mitigates the impact of the vortex on the flow channel blockage. In contrast, the vortex and cavitation in the rotating domain are more prone to accumulation in the blade region subsequent to their generation. Concurrently, in the context of rotary machinery, such as axial flow pumps, the flow channel is axial, so the vortex distributed along the circumferential direction are more prone to obstruct the flow channel, and impacting the performance of the equipment. The characteristics of vortex and cavitation in rotational and translational domain hydraulic machinery exhibit both similarities and differences. If we want to improve the performance and service life of the equipment by optimizing the structure, we must take into account the type of the domain, and we can not mistakenly apply the results of the translational domain to the rotational domain. However, there are still many contents that we haven't research. For example, under extreme working conditions, the cavitation and vortex characteristics of the two may be different. The equipment used in the case of rotation domain in this paper is designed with reference to axial flow pumps, and the situation may be different for other rotational domain hydraulic machinery, such as centrifugal pumps.

6. Conclusions

The STAR-CCM+ software was utilized for mesh generation and flow field simulation. Experiments conducted by Dreyer *et al.* [27, 28] and our grid independence verification demonstrated that the simulation effect of the 3.4 million grid was optimal and the computing power consumption was minimal. Subsequently, this grid was employed to simulate the flow field at various speeds, and the simulation of the hydrofoil in the translational domain was introduced for comparative analysis. The conclusions are as follows:

- Both the rotational domain and the translational domain exhibit a multitude of identical vortices, including TLV, TSV, and S-TLV. However, there is a distinction exists between PV, which forms at the tail of the translational domain due to the entrainment of TLV, and TEV, which is generated at the trailing edge of the rotational domain due to centrifugal force.
- The strength of the TLV is initially weak; however, it continuously absorbs other vortices, which enhances its strength during the process of backward development.
- In order to generate the identical vortices and cavitation in the rotational domain, a higher speed is necessary. This requirement arises from the uneven velocity distribution in the radial direction within the rotational domain. As the speed increases, the AC distribution will be gradually develop from the outer region toward the inner region.

- AC does not significantly influence the generation of TLVC. This is because TLV exerts a repelling effect on the AC at the suction surface. The generation of TLVC primarily depends on TLV for the absorption of TSVC from the gap.
- In comparison to the rotational domain, the translational domain is easier to form vortices and cavitation. However, due to the inherent structural differences between the two domains, vortices in the rotational domain exhibit a more pronounced blockage effect on the flow channel. In contrast, in the translational domain, the inlet flow effectively removes cavitation from the surface of the hydrofoil, thereby mitigating its impact.

Acknowledgment

This research was funded by the Qing Lan Project of Jiangsu Province, the Natural Science Foundation of the Jiangsu Higher Education Institutions of China (23KJD460008) and the industry-university- research Cooperation Project of Jiangsu Province (DH20230947).

Nomenclature

c	– chord length, [mm]	V	– water velocity, [m·s^{-1}]
F	– lift force, [N]	V_{inlet}	– inlet velocity, [m·s^{-1}]
F_{vap}	– evapouration coefficient, [–]	V_{tip}	– blade tip velocity, [m·s^{-1}]
F_{cond}	– condensation coefficient, [–]	$V_{c\infty}$	– theoretical circumferential velocity, [m·s^{-1}]
k	– turbulence kinetic energy, [m^2·s^{-2}]	V_r	– radial velocity, [m·s^{-1}]
$\dot{m}^+$	– evaporation rate, [%]	*Greek symbols*	
$\dot{m}^-$	– condensation rate, [%]	α	– angle of attack, [°]
n	– revolving speed, [r·min^{-1}]	α_l	– water volume fraction, [–]
n_0	– seed density, [–]	α_{v}	– vapour volume fraction, [–]
P_k	– the turbulence generation term caused by viscous force, [kg·m^{-1}·s^{-3}]	ε	– turbulence dissipation rate, [%]
p	– pressure, [Pa]	μ	– dynamic viscosity, [Pa·s]
p_0	– working pressure, [Pa]	μ_{t}	– turbulent viscosity, [Pa·s]
p_{outlet}	– outlet pressure, [Pa]	ρ	– density, [kg·m^{-3}]
p_{v}	– saturated vapour pressure, [Pa]	ω	– specific dissipation rate, [s^{-1}]
Q	– Q criterion, [s^{-2}]	*Subscripts*	
R_{b}	– the radius of a single bubble, [m]	l	– liquid
t	– time, [s]	v	– vapour
u	– velocity, [m/s]	mag	– magnitude

References

[1] Xie, Y., *et al*., Analysis of Unstable Hydrofoil Energy-Capturing Motion Due to Energy Dissipation, *Polish Journal of Environmental Studies, 27* (2018), 5, pp. 2315-2324

[2] Xu, J., *et al*., Numerical Analysis of Leading-Edge Vortex Effect on Tidal Current Energy Extraction Performance for Chord-Wise Deformable Oscillating Hydrofoil, *Journal of Marine Science and Engineering, 7* (2019), 11, 398

[3] Zhang, H., *et al*., Experimental Investigation of fluid-structure interaction of composite hydrofoils in cavitating flow, *Journal of Hydrodynamics, 34* (2022), pp. 207-213

[4] Liu, J., *et al*., Numerical investigation of shedding dynamics of cloud cavitation around 3D hydrofoil using different turbulence models, *European Journal of Mechanics B-fluids, 85* (2021) pp. 232-244
[5] Liu, Y., *et al*., Investigation on the dynamic behavior of cloud cavitation around a flexible hydrofoil, *Journal of Hydrodynamics, 35* (2023), pp. 712-723
[6] Dular, M., *et al*., Relationship between cavitation structures and cavitation damage, *Wear, 257* (2004), 11, pp. 1176-1184
[7] Kumagai, I., *et al*., Bubble Generation by a Cylinder Moving Beneath a Free Surface, *Journal of Fluid Science and Technology, 6* (2011), 6, pp. 851-859
[8] Kumagai, I., *et al*., Power-saving device for air bubble generation using a hydrofoil to reduce ship drag: Theory, experiments, and application to ships, *Ocean Engineering, 95* (2015), 1, pp. 183-194
[9] Murai, Y., *et al*., Mechanism and performance of a hydrofoil bubble generator utilized for bubbly drag reduction ships, *Ocean Engineering, 216* (2020), 15, 108085
[10] Zhang D., *et al*., Numerical analysis of the unsteady cavitation shedding flow around twisted Hydrofoil based on hybrid filter model. *Thermal Science*, 22, 2018, 4, pp. 1629-1636.
[11] Zang, J., *et al*., Analysis of cavity shedding around the twisted hydrofoil, *Thermal Science, 27* (2023), 4A, pp. 2593-2605
[12] Zhang Y., *et al*., Transient analysis of a noise suppression method with aerating techniques in capillary tubes, *Thermal Science*, 27, 2023, 6A, pp. 4637-4649.
[13] Hutli E., *et al*., Study and analysis of the cavitating and non-cavitating jets - Part one: Parameters controlling force, power and the jet behavior, *Thermal Science*, 24, 2020, 1A, pp. 393-406.
[14] Qin, D., *et al*., Numerical simulation of vortex instabilities in the wake of a preswirl pumpjet propulsor, *Physics of Fluids, 33* (2021), 5, 055119
[15] Zhang, W., *et al*., Effects of an Inlet Vortex on the Performance of an Axial-Flow Pump, *Energies, 13* (2020), 11, 2854
[16] Zhang, Y., *et al*., Analysis of the vortices in the inner flow of reversible pump turbine with the new omega vortex identification method, *Journal of Hydrodynamics, 30* (2018), pp. 463-469
[17] Zhang, W., *et al*., Identification and analysis of the inlet vortex of an axial-flow pump, *Journal of Hydrodynamics, 34* (2022), pp. 234-243
[18] Shi, J., *et al*., Effect of Gas Volume Fraction on the Energy Loss Characteristics of Multiphase Pumps at Each Cavitation Stage, *Water, 13* (2021), 16, 2293
[19] Song, X., *et al*., Study on the Vortex in a Pump Sump and Its Influence on the Pump Unit, *Journal of Marine Science and Engineering, 11* (2022), 1, 103
[20] Long, Y., *et al*., Research on Cavitation Wake Vortex Structures Near the Impeller Tip of a Water-Jet Pump, *Energies, 16* (2023), 4, 1576
[21] Lu, J., *et al*., Numerical and experimental investigation on the development of cavitation in a centrifugal pump, *Proceedings of the Institution of Mechanical Engineers, Part E: Journal of Process Mechanical Engineering, 230* (2016), 3, pp. 171-182
[22] Lu, J., *et al*., Investigation on the vibration and flow instabilities induced by cavitation in a centrifugal pump, *Advances in Mechanical Engineering, 9* (2017), 4

[23] Zhao, W., *et al*., .An active method to control cavitation in a centrifugal pump by obstacles, *Advances in Mechanical Engineering, 9* (2017), 11
[24] Menter F. R., Two-equation eddy-viscosity turbulence models for engineering applications. AIAA Journal, 32 (1994), 8, pp. 1598-1605.
[25] Sauer, J., Schnerr, G. H., Unsteady Cavitating Flow-A New Cavitation Model Based on a Modified Front Capturing Method and Bubble Dynamics, *Proceedings,* ASME Fluid Engineering Summer Conference, Boston, Mass., USA, 2000
[26] Siemens AG, Simcenter STAR-CCM+ User Guide version 2023.6., Siemens AG, Munich, Germany, 2023.
[27] Dreyer, M., Mind The Gap: Tip Leakage Vortex Dynamics and Cavitation in Axial Turbines, Ph. D. thesis, EPFL, Lausanne, Switzerland, 2015
[28] Dreyer, M., et al. Mind the gap: a new insight into the tip leakage vortex using stereo-PIV. *Experiments in Fluids*, 55 (2014), 1849
[29] Zhang, H., *et al.*, Numerical Analysis of the Effect of avitation on the Tip Leakage Vortex in an Axial-Flow Pump, *Journal of Marine Science and Engineering*, *9* (2021), 7, 775
[30] Shen, S., *et al*., Numerical investigation of tip flow dynamics and main flow characteristics with varying tip clearance widths for an axial-flow pump, *Proceedings of the Institution of Mechanical Engineers, Part A: Journal of Power and Energy, 233* (2019), 4, pp. 476-488
[31] Zhang, H., *et al*., Analysis of the Formation Mechanism of Secondary Tip Leakage Vortex (S-TLV) in an Axial Flow Pump, *Machines, 10* (2022), 1, 41
[32] Zhang, D., *et al*., Numerical analysis of unsteady tip leakage vortex cavitation cloud and unstable suction-side-perpendicular cavitating vortices in an axial flow pump, *International Journal of Multiphase Flow, 77* (2015), pp. 244-259
[33] Shi, L., *et al.*, Visualized observations of trajectory and dynamics of unsteady tip cloud cavitating vortices in axial flow pump, *Journal of Fluid Science and Technology, 12* (2017), 1
[34] Zhang, H., *et al*., Analysis of the Formation Mechanism and Evolution of the Perpendicular CavitationVortex of Tip Leakage Flow in an Axial-Flow Pump for Off-Design Conditions, *Journal of Marine Science and Engineering*, *9* (2021), 10, 1045
[35] Che, B., *et al*., Control effect of micro vortex generators on leading edge of attached cavitation, *Physics of Fluids, 31* (2019), 4, 044102

Submitted: 14.07.2024.

Revised: 10.12.2024.

Accepted: 16.12.2024.